*Journal of Adhesion Science and Technology 26 (2012) 1825–1851*

# A Phase-Field Based Hybrid Lattice-Boltzmann Finite-Volume Method and Its Application to Simulate Droplet Motion under Electrowetting Control

**J.J. Huang**[1], **C. Shu**[2,*], **J.J. Feng**[3,4] **and Y.T. Chew**[2]
[1] Temasek Laboratories, National University of Singapore,
5A Engineering Drive 1, Singapore 117411, Singapore
[2] Department of Mechanical Engineering, National University of Singapore,
10 Kent Ridge Crescent, Singapore 119260, Singapore
[3] Department of Chemical and Biological Engineering, University of British Columbia,
Vancouver, BC V6T 1Z3, Canada
[4] Department of Mathematics, University of British Columbia,
Vancouver, BC V6T 1Z2, Canada

**Abstract**

A phase-field based numerical model combining the lattice-Boltzmann method (LBM) and the finite-volume method (FVM) is proposed and applied for the study of two-dimensional (2-D) droplet under electrowetting (EW) control by using alternating current (AC). The new model overcomes several limitations of the pure LBM in interface dynamics, while keeping the key advantages of LBM for hydrodynamics. The model formulation is presented and some numerical issues are discussed. Droplet motions under EW control are investigated by using this method, with the focus on the effects of key control parameters on the induced droplet oscillation. This study may provide useful guidelines for mixing enhancement within the droplet by EW control.

**Keywords**: *Droplet Oscillation*, *Electrowetting*, *AC control*, *Phase-Field Model*, *Lattice-Boltzmann Method*, *Finite-Volume Method*.

*Corresponding author. E-mail: mpeshuc@nus.edu.sg

# 1 Introduction

Microfluidic systems promise to revolutionize the chemical and biological laboratories, and thus have attracted considerable attention in recent years [1]. Droplet actuation, transport, and mixing within the droplets are all encountered in such systems. One of the effective methods to control droplets is electrowetting (EW) [2, 3]. To optimize the design and operation of EW controlled microfluidic systems, computer simulation plays a very important role. In general, EW modeling and simulation may be categorized into two types: the quasi-static (QS) approach and the full computational fluid dynamics (CFD) simulation [4]. The QS approach assumes that droplet is in its quasi-static limit and minimizes the total energy of the system subject to EW and various constraints to find the droplet shape. By contrast, a full CFD simulation includes much more physics and is more realistic, but it is computationally much more demanding.

Electrowetting controlled droplets have been investigated by both numerical and experimental methods recently. Walker et al. [5] proposed a Hele-Shaw type model to study the droplets confined between two parallel plates with EW control. They included the contact line pinning effect and obtained good agreement between numerical and experimental results. However, they mainly focused on translational motions of the droplet. Oh et al. [6, 7] developed a numerical model based on the domain perturbation method to study droplet oscillations under AC-controlled EW. Although quite efficient, their model is restricted only to small deformation of the droplet. Lu et al. [8] proposed a diffuse-interface model to study droplet motion in a Hele-Shaw cell, and provided asymptotic analysis for its sharp-interface limit. Their prediction of droplet deformation agrees well with experiment. Aminfar and Mohammadpourfard [9] proposed a free energy-based lattice-Boltzmann model for droplet under EW. They solved the Poisson-Boltzmann equation for the electrical potential and showed that its solution is effectively one-dimensional under usual conditions. Only DC-controlled droplets were considered in [8] and [9]. In recent years, more experiments have been carried out to study AC-controlled droplets [10, 6, 11, 12, 13]. Mugele et al. [10] studied mixing by EW-induced droplet oscillations and found that such oscillations may greatly enhance mixing. Oh et al. [6] investigated droplet oscillations systematically and discovered certain resonance frequencies and different oscillation modes. Ko et al. [11] studied the hydrodynamic flows inside oscillating droplets through flow visualization, and uncovered two types of flows in different frequency ranges. Lai et al. [12] reported the oscillation spectrums and beat phenomenon of a water droplet under AC EW, and also highlighted the phase difference between the applied voltage and droplet motion. Recently, Ko et al. [13] examined an interesting method to generate jets from EW-controlled oscillating bubbles. Probably because of computational difficulties, the numerical investigations of AC-controlled droplet oscillations seem to lag behind the corresponding experimental studies.

Mixing is an important process in microfluidic devices for chemical and biological applications. However, as is well known, mixing is more difficult at small scales than at large scales because of the weak advection at low Reynolds numbers. As mentioned above, one method to enhance mixing at small scales is through EW-controlled droplet oscillation [14, 15, 10]. To understand this process, one must know the details of the dynamic flow fields inside the droplet, which are often difficult to obtain in experiments. Numerical simulations can be very helpful in this respect. However, it is a rather daunting challenge because of the complex processes occurring simultaneously (namely, two-phase flows, wetting and electrowetting, and mixing due to convection-diffusion).

In this paper, we focus on CFD simulations of droplets under AC-controlled EW. The long-term aims of the present work include the investigation of mixing inside such droplets, which can be handled by CFD simulations but not by the QS approach. Previous numerical studies of this type of flows usually employed *front-tracking* methods that are not very flexible in handling topological changes. Here, we propose a phase-field (or diffuse-interface) method and apply it to study an AC-controlled droplet. Unlike previous studies that used sinusoidal waveforms for the voltage, we use a trapezoidal waveform for voltage with several stages of controlled durations (details to be given later). This introduces extra dimensions for voltage control and might lead to more efficient mixing. As a first step, we focus on the oscillation of the drop and the flow field inside, with the aim of approximating the droplet motion observed in mixing enhancement experiments (see [10]). Mixing itself, described by an additional advection-diffusion equation, will be investigated in a future effort.

In the literature, there are several *full* CFD simulation methods for multiphase flows encountered in microfluidics, in which both phases are simultaneously considered, including the front-tracking method, volume-of-fluid method, level-set method and the phase-field or diffuse-interface method. There are two common requirements for computational methods to simulate multiphase flows,

- to capture or track the interface motion;
- to model the interfacial tension effects and their coupling with the flow.

In a continuum formalism, accordingly, two sets of equations need to be solved: one for the interface motion and the other for the fluid flow (often the Navier-Stokes equations (NSEs) with additional term for the interfacial tension).

In addition to these continuum-based methods, there is a *quasi-particle* method known as the lattice-Boltzmann method (LBM). LBM for multiphase flows has undergone substantial development in the past two decades and has seen successful applications for many problems. One of the popular models in LBM, the free-energy based LBM, is closely connected with the phase-field method. In most free energy-based LBMs, two sets of distribution functions are used to simulate the phenomena that are described by the two sets of equations in the continuum-based methods. The success of LBM is due to some special features, including its simplicity and excellent parallel performance. Besides, in LBM there is no need to solve the Poisson equation for pressure, and complex geometries such as those in porous media can be treated in a relative easy manner. However, there are some issues in the popular free energy-based lattice-Boltzmann models using two sets of distribution functions. Firstly, the relaxation parameter for the set of distribution functions that describe the interface is not fixed but often empirically determined, and using different values may lead to different results. Secondly, the equation for the interface often differs from that in the phase-field model (to be more specific, the Cahn-Hilliard equation (CHE)) with extra terms. Some efforts have been made to devise an *optimal* lattice-Boltzmann equation that closely follows the CHE (e.g., see [16]). Thirdly, it is difficult to use a variable mobility (in the CHE) in the LBM framework. Fourthly, the boundary conditions for the variables in the CHE are implemented indirectly through the distribution functions. This is less straightforward and might not be accurate enough in some cases. Fifthly, the lattice-Boltzmann equation typically uses $2^{nd}$-order explicit time stepping, which may require very small time steps for the CHE. All these issues are related to the interface equation. To overcome them while keeping the advantageous features of LBM, we propose a hybrid method that integrates LBM for fluid flow and the finite-volume method (FVM) for interface dynamics. As a new computational scheme, we establish the theoretical and numerical framework in this paper, without attempting to address all the numerical issues listed above. For instance, we will use a constant mobility for simplicity. In spirit, our approach resembles the LBM-finite-difference hybrid method of Tiribocchi et al. [17].

The paper is organized as follows. In Section 2, the theoretical model and the hybrid method are described. In Section 3, the specific problem studied is presented, some numerical issues in the phase-field model are discussed, the EW control is then introduced, and finally a few specific studies of different parameters are carried out. Section 4 concludes this paper.

## 2 Theoretical Model and Numerical Methodology

The present method is based on the phase-field model for binary fluids. As mentioned earlier, there are two types of dynamics being considered, hydrodynamics for fluid flow and interfacial dynamics, which are closely coupled together. The lattice-Boltzmann method is employed to simulate the hydrodynamics, whereas the equation describing the interface motion, the Cahn-Hilliard equation, is solved by the finite-volume method (for spatial discretization) and the Runge-Kutta method for time marching. These components are described in the following subsections.

## 2.1 Phase-Field Model

In the phase-field model, an order parameter $\phi$ is used to distinguish different fluids, and a free energy functional is defined as

$$\mathcal{F}(\phi, \boldsymbol{\nabla}\phi) = \int_V \left( \Psi(\phi) + \frac{1}{2}\kappa |\boldsymbol{\nabla}\phi|^2 \right) dV + \int_S \varphi(\phi) dS \tag{2.1}$$

where $\Psi(\phi)$ is the *bulk free energy* density and takes the form

$$\Psi(\phi) = a(\phi^2 - 1)^2 \tag{2.2}$$

with $a$ being a constant. This form indicates that $\phi$ varies between $-1$ (in one fluid) and 1 (in the other fluid). The second term is the *interfacial energy* density with $\kappa$ being another constant, and the last term in the surface integral is the *surface energy* density. In this work, we use the following surface energy [18],

$$\varphi(\phi) = -\sigma \cos\theta \frac{\phi(3 - \phi^2)}{4} + \frac{1}{2}(\sigma_{w1} + \sigma_{w2}) \tag{2.3}$$

where $\sigma$ is the interfacial tension between the two fluids, $\theta$ is the static contact angle, $\varphi(\pm 1)$ gives the fluid-solid interfacial tensions $\sigma_{w1}$ and $\sigma_{w2}$ between the wall and fluid 1 and fluid 2, respectively. Young's equation determines $\theta$ as

$$\cos\theta = \frac{\sigma_{w2} - \sigma_{w1}}{\sigma} \tag{2.4}$$

The chemical potential $\mu$ is calculated by taking the variation of the free energy functional with respect to the order parameter,

$$\mu = \frac{\delta \mathcal{F}}{\delta \phi} = \frac{d\Psi(\phi)}{d\phi} - \kappa \nabla^2 \phi = 4a\phi(\phi^2 - 1) - \kappa \nabla^2 \phi. \tag{2.5}$$

The coefficients $a$ and $\kappa$ can be related to the interfacial tension $\sigma$ and interface width $W$ as [19],

$$a = \frac{3\sigma}{4W}, \tag{2.6}$$

$$\kappa = \frac{3\sigma W}{8}. \tag{2.7}$$

## 2.2 Electrowetting Modeling

To apply electrowetting to control a droplet, a common setup is to use a dielectric layer as the substrate and establish a circuit across the conductive droplet [3, 10] (known as *electrowetting-on-dielectric*). In such a electrowetting system after a voltage $V$ is applied, the new equilibrium static contact angle $\theta$ may be expressed as [4]

$$\cos\theta = \frac{\sigma_{\mathrm{w2}} - \sigma_{\mathrm{w1}} + \frac{1}{2}\frac{\varepsilon_r \varepsilon_0}{d} V^2}{\sigma} \tag{2.8}$$

where $\sigma$, $\sigma_{\mathrm{w1}}$ and $\sigma_{\mathrm{w2}}$ are defined above,

$d$ is the thickness of the dielectric layer (substrate), $\varepsilon_r$ is the relative dielectric constant of the material, and $\varepsilon_0$ is the dielectric constant of vacuum. This equation suggests that the effect of the applied voltage can be absorbed into either $\sigma_{\mathrm{w1}}$ or $\sigma_{\mathrm{w2}}$ to form an *equivalent interfacial tension* [4] (for instance, an equivalent $\sigma_{\mathrm{w1}}(V)$ with the electrostatic energy taken into account may be defined as $\sigma_{\mathrm{w1}} - \frac{1}{2}\frac{\varepsilon_r \varepsilon_0}{d} V^2$). In terms of the zero-voltage contact angle, the contact angle at voltage $V$ may be expressed as

$$\theta(V) = \cos^{-1}\left[ \cos[\theta(0)] + \frac{\frac{1}{2}\frac{\varepsilon_r \varepsilon_0}{d} V^2}{\sigma} \right]. \tag{2.9}$$

A more sophisticated approach is to include the electrical potential in the system and solve for the potential, which is governed by the Poisson-Boltzmann equation [9]. However, unless the system is extremely small (e.g.,

at nanometer scale for which the Debye length is non-negligible), the potential distribution in the droplet can be much simplified and the contribution due to the electrical field may be captured by the boundary conditions (e.g., through the surface energy term) [9].

As noted in Section 1, we are interested in dynamic situations with the contact angle controlled by AC, in which the voltage varies with time, i.e., $V = V(t)$. A straightforward extension of Eq. (2.9) gives

$$\theta(V(t)) = \cos^{-1}\left[\cos[\theta(0)] + \frac{\frac{1}{2}\frac{\varepsilon_r\varepsilon_0}{d}[V(t)]^2}{\sigma}\right]. \tag{2.10}$$

We assume that by specifying the *instantaneous equilibrium contact angle* in phase-field simulations, one may *approximately* mimic the dynamics of the system subject to the AC-controlled electrowetting.

Detailed specification of the parameters $d$, $\varepsilon_r$, and $\varepsilon_0$ may be avoided if the equilibrium contact angle under the maximum voltage $V_M$ is known.

Thus, the coefficient in front of $V^2$ can be determined:

$$\frac{\varepsilon_r\varepsilon_0}{d} = \frac{2\sigma}{V_M^2}\left(\cos[\theta(V_M)] - \cos[\theta(0)]\right). \tag{2.11}$$

## 2.3 Lattice-Boltzmann Method for Hydrodynamics

For the fluid flow, the lattice-Boltzmann method is used to simulate the hydrodynamics. The lattice-Boltzmann equation reads [19],

$$f_i(\boldsymbol{x} + \boldsymbol{e}_i\delta_t, t + \delta_t) - f_i(\boldsymbol{x}, t) = -\frac{1}{\tau_f}[f_i(\boldsymbol{x}, t) - f_i^{eq}(\boldsymbol{x}, t)] + \frac{1}{c_s^2}\delta_t w_i \boldsymbol{e}_i \cdot [\mu\boldsymbol{\nabla}\phi] \tag{2.12}$$

where $\boldsymbol{e}_i$ $(i = 0, 1, \cdots, b)$ is the lattice velocity and for the D2Q9 model used here,

$$\boldsymbol{e}_i = \begin{cases} 0 & \text{for } i = 0 \\ (\cos[\frac{(i-1)\pi}{4}], \sin[\frac{(i-1)\pi}{4}])c & \text{for } i = 1, 2, \cdots, 8 \end{cases} \tag{2.13}$$

with $c$ being the lattice velocity, $\delta_t$ is the time step ($\delta_x = c\delta_t$ is the grid spacing), $c_s$ is the *LBM sound speed*. The equilibrium distribution $f_i^{eq}$ is given by

$$f_i^{eq} = w_i\left\{A_i + \rho\left[\frac{1}{c_s^2}\boldsymbol{e}_i \cdot \boldsymbol{u} + \frac{1}{2c_s^4}(\boldsymbol{e}_i \otimes \boldsymbol{e}_i - c_s^2\mathbf{I}) : (\boldsymbol{u} \otimes \boldsymbol{u})\right]\right\} \tag{2.14}$$

with $w_i$ being the weight for different lattice velocities,

$$w_i = \begin{cases} \frac{4}{9} & \text{for } i = 0 \\ \frac{1}{9} & \text{for } i = 1, 3, 5, 7 \\ \frac{1}{36} & \text{for } i = 2, 4, 6, 8 \end{cases} \tag{2.15}$$

$\rho$ being the density (nearly a constant), and the coefficient $A_i$ is given by

$$A_i = \begin{cases} A = \frac{1}{c_s^2}(\rho c_s^2 + \phi\mu) & \text{if } i > 0 \\ \frac{1}{w_0}[\rho - (1 - w_0)A] & \text{if } i = 0 \end{cases} \tag{2.16}$$

The last term (combined with the specially designed equilibrium distributions) provides the force due to the interfacial tension. The second-order moments of $f_i^{eq}$ satisfy the following relation,

$$\sum_{i=0}^{b} e_{i_\alpha} e_{i_\beta} f_i^{eq} = \rho u_\alpha u_\beta + (\rho c_s^2 + \phi\mu)\delta_{\alpha\beta} \tag{2.17}$$

where the subscripts $\alpha$ and $\beta$ denote the spatial coordinate directions. The density and momentum are calculated as,

$$\rho = \sum_{i=0}^{b} f_i, \quad \rho \boldsymbol{u} = \sum_{i=1}^{b} f_i \boldsymbol{e}_i$$

The relaxation parameter $\tau_f$ is related to the viscosity of the fluid. Using the Chapman-Enskog expansion, the following equation can be obtained in the long-time, large-wavelength limit,

$$\frac{\partial}{\partial t}(\rho \boldsymbol{u}) + \boldsymbol{\nabla} \cdot [\rho \boldsymbol{u} \otimes \boldsymbol{u} + (\rho c_s^2 + \phi \mu)\mathbf{I}] = \boldsymbol{\nabla} \cdot [\rho \nu (\boldsymbol{\nabla} \boldsymbol{u} + (\boldsymbol{\nabla} \boldsymbol{u})^T)] + \mu \boldsymbol{\nabla} \phi \tag{2.18}$$

where $\nu$ is the kinematic viscosity and it is related to $\tau_f$ as

$$\nu = c_s^2(\tau_f - 0.5)\delta_t \tag{2.19}$$

Note that for very small *LBM Mach number* $M_{\text{LBM}} = \frac{|\boldsymbol{u}|_{\max}}{c_s}$ ($|\boldsymbol{u}|_{\max}$ is the maximum velocity magnitude) (which is well satisfied in this work), Eq. (2.18) approximates the following incompressible Navier-Stokes equations (NSEs) sufficiently well,

$$\frac{\partial \boldsymbol{u}}{\partial t} + (\boldsymbol{u} \cdot \boldsymbol{\nabla})\boldsymbol{u} = -\boldsymbol{\nabla} S + \nu \nabla^2 \boldsymbol{u} - \phi \boldsymbol{\nabla} \mu \tag{2.20}$$

where $S$ is similar to the hydrodynamic pressure in the usual situation without any interfacial tension [20].

Near the wall, the bounce-back-by-link (BBL) condition is applied for $f_i$.

## 2.4 Finite-Volume Method for Interface Dynamics

As noted before, the interface dynamics is described in terms of the order parameter $\phi$ field, which is governed by the Cahn-Hilliard equation [20],

$$\frac{\partial \phi}{\partial t} + (\boldsymbol{u} \cdot \boldsymbol{\nabla})\phi = \boldsymbol{\nabla} \cdot (M \boldsymbol{\nabla} \mu) \tag{2.21}$$

where $M$ is the mobility. For incompressible flow, $\boldsymbol{\nabla} \cdot \boldsymbol{u} = 0$, and it may be rewritten as

$$\frac{\partial \phi}{\partial t} = \boldsymbol{\nabla} \cdot (-\boldsymbol{u}\phi + M \boldsymbol{\nabla} \mu) \tag{2.22}$$

Note that Eq. (2.5) is required to calculate the chemical potential in Eq. (2.22).

### 2.4.1 FVM mesh and its relation to LBM mesh

For a clear description, it is helpful to first introduce the mesh for the finite-volume method. The relation between the FVM mesh and the LBM mesh is shown in Figure 1. Note that when the bounce-back-by-link (BBL) condition is used in LBM for $f_i$, the outmost LBM nodes are half-lattice ($\frac{\delta_x}{2}$) away from the wall. By using the arrangement in Figure 1, the boundary of the FVM mesh overlaps with the wall. This allows for an easier enforcement of the boundary conditions for $\phi$ and $\mu$ (as shown later).

### 2.4.2 Spatial discretization by FVM

For a square cell with four sides 1, 2, 3, and 4, the finite-volume discretizations of Eqs. (2.22) and (2.5) read,

$$\frac{d}{dt}(V_\Omega \bar{\phi}) = \sum_{k=1}^{4} \int_k \left( -u_n \phi + M \frac{\partial \mu}{\partial n} \right)_k dS \tag{2.23}$$

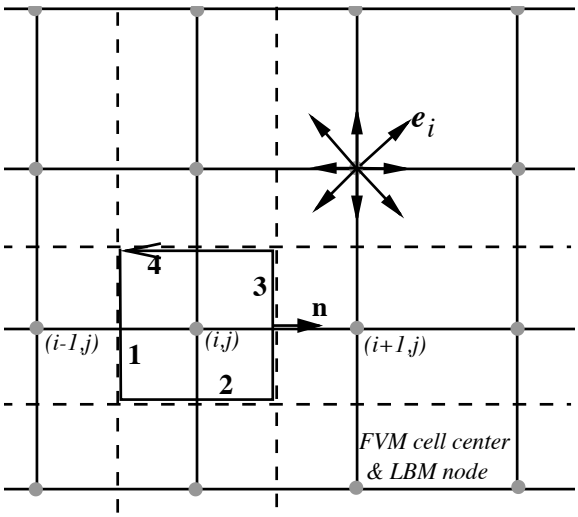


Figure 1: Mesh for coupling LBM and FVM (solid line with filled circle: LBM mesh; dashed line: FVM mesh; line with arrow and labels "1, 2, 3, 4": boundary of one cell in FVM along the direction of integral; 1, 2, 3, 4: four sides of a cell in FVM; $\boldsymbol{n}$: local outward normal vector of a FVM cell boundary (on side 3); filled circle: LBM node and also the cell center in FVM; $\boldsymbol{e}_i$: lattice velocity).

$$\bar{\mu} = \overline{\Psi'(\phi)} + \frac{\kappa}{V_\Omega} \sum_{k=1}^{4} \int_k \left( \frac{\partial \phi}{\partial n} \right)_k dS \tag{2.24}$$

where $\boldsymbol{n}$ is the outward unit normal vector along the boundary of the cell, $u_n$ is the projection of the velocity on $\boldsymbol{n}$, $\frac{\partial \mu}{\partial n}$ and $\frac{\partial \phi}{\partial n}$ are the normal derivatives of the chemical potential and order parameter respectively, $\bar{\phi} = \frac{1}{V_\Omega} \int_\Omega \phi d\Omega$, $\bar{\mu} = \frac{1}{V_\Omega} \int_\Omega \mu d\Omega$, and $\overline{\Psi'(\phi)} = \frac{1}{V_\Omega} \int_\Omega \Psi'(\phi) d\Omega$ are the the cell-averaged values of $\phi$, $\mu$, and $\Psi'(\phi)$ respectively, $\int_k$ denotes integral along side $k$ with appropriate direction (counter-clockwise). In this work, we approximate the term $\overline{\Psi'(\phi)}$ as $\overline{\Psi'(\phi)} \approx \Psi'(\phi)|_{\phi=\bar{\phi}}$. Other terms in Eqs. (2.23) and (2.24) involve the integrals along the faces (sides) of the cell. They are calculated as the average of the values in two neighbouring cells. For instance, for the convection term $-u_n\phi$ on side 3, the integral is calculated as,

$$\int_3 (-u_n\phi)_3 dS = \frac{1}{2} \left( \int_{(i,j)} (-u_n\phi)_{(i,j)} dS + \int_{(i+1,j)} (-u_n\phi)_{(i+1,j)} dS \right) \tag{2.25}$$

where $\int_{(i,j)}$ means the integral is performed in the cell $(i,j)$. Note that along side 3, $dS = dy$, $u_n = u$. For the cell $(i,j)$, the integral is approximated along the center vertical line, and also rewritten in the local coordinate $\xi = \frac{1}{\delta_x}(y - y_{i,j})$ Then, it becomes,

$$\int_{(i,j)} (-u_n\phi)_{(i,j)} dS = \delta_x \int_{-0.5}^{0.5} [-u(\xi)\phi(\xi)]_{(i,j)} d\xi \tag{2.26}$$

The local profiles $u(\xi)$ and $\phi(\xi)$ along the center line are reconstructed using one local and two neighbouring (cell-averaged) values. For instance, $\phi = \phi(\xi)$ is found from $\bar{\phi}_{i,j-1}$, $\bar{\phi}_{i,j}$, $\bar{\phi}_{i,j+1}$ as,

$$\phi(\xi) = a\xi^2 + b\xi + c \tag{2.27}$$

with

$$c = \bar{\phi}_{i,j}, \quad b = \frac{1}{2}(\bar{\phi}_{i,j+1} - \bar{\phi}_{i,j-1}), \quad a = \frac{1}{2}(\bar{\phi}_{i,j+1} + \bar{\phi}_{i,j-1} - 2\bar{\phi}_{i,j}) \tag{2.28}$$

Similar reconstructions are applied for $u_n$ and $\mu$ as well. Using such reconstructions, the accuracy in the direction parallel to each side can reach $3^{rd}$-order in theory, and the accuracy in the normal direction is $2^{nd}$-order. Overall, at least $2^{nd}$-order accuracy can be guaranteed. The integrals for the normal derivatives are

calculated in a somewhat different way. For example, along side 3,

$$\int_3 \left(\frac{\partial \phi}{\partial n}\right)_3 dS = \int_3 \frac{\partial \phi}{\partial x} dy \approx \delta_x \int_3 \frac{\phi_{i+1,j}(\xi) - \phi_{i,j}(\xi)}{\delta_x} d\xi \tag{2.29}$$

where $\phi_{i,j}(\xi)$ is the profile constructed along the center vertical line of the cell $(i, j)$ as given by Eqs. (2.27) and (2.28). The same formulas are used for $\mu$ as well.

### 2.4.3 Boundary conditions at the wall

At the wall, the following boundary conditions are applied for the Cahn-Hilliard equation,

$$u_{n_w} = 0 \tag{2.30}$$

$$\kappa \frac{\partial \phi}{\partial n_w} = -\varphi_w'(\phi) \tag{2.31}$$

$$\frac{\partial \mu}{\partial n_w} = 0 \tag{2.32}$$

where $\boldsymbol{n}_w$ denotes the unit normal vector at the wall (pointing into the fluid). Using Eq. (2.3), the following condition for $\phi$ is obtained,

$$\frac{\partial \phi}{\partial n_w} = \frac{3}{4}\frac{\sigma}{\kappa}\cos\theta(1 - \phi_w^2) \equiv q(1 - \phi_w^2), \tag{2.33}$$

where $\phi_w$ is the order parameter at the wall, and the parameter $q = \frac{3}{4}\frac{\sigma}{\kappa}\cos\theta$ is introduced for convenience. Note that $\phi_w$ is unknown and must be found through some relations. For consistency, the reconstruction given in Eq. (2.27) is also applied near the wall in the normal direction. Now there are four unknowns, including $\phi_w$ and the coefficients $a$, $b$ and $c$. Four relations are provided by two cell-averaged values (nearest to the wall), Eq. (2.33) (on the normal derivative) and the requirement $\phi = \phi_w$ at the wall. For instance, when side 2 overlaps with the lower wall, an equation for $\phi_w$ can be derived as,

$$\phi_w^2 + \frac{8}{3q}\phi_w - 1 + \frac{8\phi_{i,j} - (\phi_{i,j+1} - \phi_{i,j})}{-3q} = 0 \tag{2.34}$$

where $\phi_{i,j}$ takes the cell-averaged value. From this equation, two values for $\phi_w$ are found and care must be taken to select the right one. After $\phi_w$ is obtained, Eq. (2.33) can be directly used in Eq. (2.24) for the cells that have one side overlapping with the lower wall. Similarly, Eq. (2.32) can be directly used in Eq. (2.23) for such cells.

### 2.4.4 Temporal discretization

The time stepping for Eq. (2.23) employs the explicit $4^{th}$-order Runge-Kutta method. Note that the velocity is frozen during the time marching from $t^n$ to $t^{n+1}(= t^n + \delta_t)$. Eq. (2.23) can be written as,

$$\frac{d}{dt}\bar{\phi} = \frac{1}{V_\Omega}\sum_{k=1}^{4}\int_k \left( - u_n\phi + M\frac{\partial \mu}{\partial n}\right)_k dS \equiv L(\phi) \tag{2.35}$$

The time stepping follows these steps,

$$\begin{aligned}
a^n &= \delta_t L(t^n, \bar{\phi}^n) \\
b^n &= \delta_t L\left(t^n + \frac{1}{2}\delta_t, \bar{\phi}^n + \frac{1}{2}a^n\right) \\
c^n &= \delta_t L\left(t^n + \frac{1}{2}\delta_t, \bar{\phi}^n + \frac{1}{2}b^n\right) \\
d^n &= \delta_t L(t^n + \delta_t, \bar{\phi}^n + c^n)
\end{aligned} \tag{2.36}$$

$$\bar{\phi}^{n+1} = \bar{\phi}^n + \frac{1}{6}(a^n + 2b^n + 2c^n + d^n) \tag{2.37}$$

Note that Eqs. (2.23) and (2.24) are a coupled system. To advance Eq. (2.23) in time, Eq. (2.24) has to be used in each sub-step.

### 2.5 Remarks on the Hybrid Method

By using the finite-volume method for the CHE, the present hybrid method overcomes the problems with the pure LBM mentioned in Section 1, but some important LBM advantages are kept. When compared with the *conventional* Navier-Stokes methods, it avoids the need to solve the Poisson equation for the pressure. When compared with LBM using two sets of distribution functions (denoted as $f_i$ and $g_i$) for hydrodynamics and interface evolution, it is advantageous because

- It avoids introducing and adjusting the empirical relaxation parameter for the distribution functions $g_i$;
- The boundary conditions for the order parameter $\phi$ and the chemical potential $\mu$ are easily imposed accurately;
- The time stepping scheme for the Cahn-Hilliard equation is more flexible (for instance, schemes with better stability properties like high-order Runge-Kutta schemes or even semi-implicit schemes may be used).
- It makes it easier to use a variable mobility $M(\phi)$ (dependent on the order parameter);
- The hybrid framework allows easier inclusion of more physical phenomena, for example, the convection-diffusion of some additional species within the droplet (which is encountered when considering mixing inside the droplet).

Note that the third aspect about time stepping becomes more important as the interfacial thickness $W$ (reflected by the Cahn number $Cn$ to be defined later) decreases. The Cahn-Hilliard equation becomes stiffer at smaller $Cn$ and imposes more stringent requirement on $\delta_t$.

Of course, the hybrid formulation is more complex than each of the constituent ones. But when compared with the pure LBM formulation, the increased complexity is not significant because the solution of the Cahn-Hilliard equation consumes a relatively small portion of the overall effort. As compared with the pure FVM formulation for the Navier-Stokes-Cahn-Hilliard equations, it retains the advantages of the LBM for the Navier-Stokes equations, which make up for the additional formulation complexity.

## 3 Simulation of Droplet Dynamics Under Electrowetting Control

In this section, the basic setup of the problem is given first, together with the specifications of numerical simulation. Then, various parameters in phase-field model are defined and discussed. After that, details on the temporal control of driving voltage are provided. Next, some numerical tests are performed to validate the method and also to examine the issue of convergence. Finally, case studies focusing on the effects of several control parameters are given, and some further discussions end this section.

### 3.1 Setup of the Problem and Numerical Simulation

The setup of the problem is shown in Figure 2. A droplet of radius $R$ is positioned on the lower wall, the wettability of which is controlled by electrowetting (the varying contact angle being $\theta(t)$). The droplet is

surrounded by another fluid. Note that we consider a setup in which the droplet is non-conducting whereas the surrounding fluid is conducting. When the voltage is applied, the interfacial tension between the surrounding fluid and the wall is reduced, and the contact angle $\theta$ (measured in the droplet, see Figure 2) will increase. Accordingly, one has to modify the formula from Eq. (2.10) to the following by changing the sign before the voltage term,

$$\theta(V(t)) = \cos^{-1}\left[\cos[\theta(0)] - \frac{\frac{1}{2}\frac{\varepsilon_r\varepsilon_0}{d}[V(t)]^2}{\sigma}\right]. \tag{3.1}$$

Initially, no voltage is applied and $\theta(0) = 90°$. The droplet shown in Figure 2 is at equal distance from the left and right boundaries of the domain, takes a semi-circle shape and the contact angle is 90°, thus the system is in equilibrium at that instant (this initial condition is used for all cases studied). The top wall is solid while the left and right boundaries of the domain are periodic. The computational domain has a size $L_x \times L_y$. In this work, we assume that the two fluids have the same density and viscosity for simplicity.

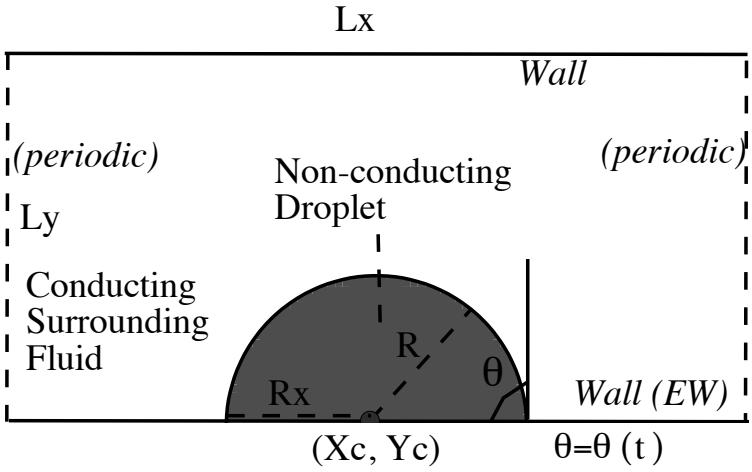


Figure 2: Problem setup for the droplet controlled by electrowetting (EW)

The interfacial tension is $\sigma$ and the kinematic viscosity is $\nu$. It is natural to use the droplet radius $R$ as the characteristic length $L_c = R$. Suppose the characteristic velocity is $U_c$, then the Reynolds number and the capillary number are defined by

$$Re = \frac{U_c L_c}{\nu} = \frac{U_c R}{\nu} \tag{3.2}$$

$$Ca = \frac{\rho\nu U_c}{\sigma} \tag{3.3}$$

However, before the simulation (or a corresponding experiment) the droplet velocity is unknown. Thus, it is not possible to determine the typical parameters like the Reynolds number and the capillary number a priori.

Following [21], we use an alternative characteristic velocity

$$U_c = \frac{\sigma}{\rho\nu} \tag{3.4}$$

Then, the characteristic time is,

$$T_c = \frac{L_c}{U_c} = \frac{R\rho\nu}{\sigma} \tag{3.5}$$

the capillary number is *always unity*, and the Reynolds number is

$$Re = \frac{U_c R}{\nu} = \frac{\sigma}{\rho\nu}\frac{R}{\nu} = \frac{\sigma R}{\rho\nu^2} \tag{3.6}$$

Of course, the dimensionless numbers calculated in this way *do not truly reflect* the physics of the problem (they may differ from the actual values by orders of magnitude, as seen later). Nevertheless, they facilitate the numerical simulation setup and the actual characteristic velocity can be found after the simulation is completed.

Note that in what follows, all quantities of length, time and velocity are scaled by $L_c$, $T_c$ and $U_c$, respectively (unless otherwise specified).

In analyzing the dynamic EW process, we will examine the following attributes of the numerical solutions:

- Droplet radius on the lower wall $R_x$, defined as half of the distance between the two three-phase points on the lower wall (see Figure 2).
- Average droplet velocity in the $y$-direction

$$\bar{V}_d = \frac{\int_V N(\phi) v dV}{\int_V N(\phi) dV} \approx \frac{\sum_{i,j} v_{i,j} N(\phi_{i,j})}{\sum_{i,j} N(\phi_{i,j})} \tag{3.7}$$

In the above, $V$ denotes the domain, and the function $N(\phi)$ is defined by

$$N(\phi) = \begin{cases} 1 & \text{if} \quad \phi > 0 \\ 0 & \text{if} \quad \phi \leq 0 \end{cases} \tag{3.8}$$

## 3.2 Parameters in Phase-Field Modeling

In the phase-field model, two additional parameters are important: the Cahn number

$$Cn = \frac{W}{L_c} \tag{3.9}$$

and the Peclet number

$$Pe = \frac{U_c L_c^2}{M\sigma}. \tag{3.10}$$

The Cahn number measures the ratio of interface width over the characteristic length (here the droplet radius), and the Peclet number reflects the ratio of convection over diffusion in the Cahn-Hilliard equation. In *real* binary fluid systems (probably except those at the nanoscale), $Cn$ is extremely small ($Cn \to 0$), $Pe$ is extremely large ($Pe \to \infty$), and the Cahn-Hilliard equation, Eq. (2.21), approaches a pure convection equation. But in phase-field modeling, both $Cn$ and $Pe$ have finite values. Usually, $Cn$ should be small enough so that the simulation results are close to the sharp-interface limit. But how to vary $Pe$ to reach such a limit is not well established in general. Recently, Yue et al. [18] studied the convergence of numerical results towards a sharp-interface limit in terms of an alternative parameter $S$ defined by

$$S = \frac{\sqrt{M\nu}}{L_c}. \tag{3.11}$$

They provided guidelines on how to approach the sharp-interface limit by varying these parameters in phase-field simulations. A brief study on convergence will be provided later in Subsection 3.5.

## 3.3 Control of the Driving Voltage

The modeling of electrowetting was presented in Subsection (2.2). Since we consider AC control and the voltage is time-dependent, the form of voltage variation has to be specified. It is important to determining the droplet deformation. In fact, it is one of the main factors studied in this work.

Suppose the voltage varies with time as

$$V(t) = V_M f_V(t; T_{\text{EW}}) \tag{3.12}$$

where $T_{\text{EW}}$ is a characteristic time scale for the electrowetting control (e.g., the AC period), and $f_V$ satisfies $0 \leq f_V(t) \leq 1$. In the above, it is assumed that the applied voltage $V$ acts instantly (e.g., on a time scale much

smaller than $T_{\rm EW}$), and is within the range for *electrowetting-on-dielectric* to work. In other words, a quasi-static balance is assumed to hold at each moment between the surface energies and the electrical potential [8].

Consider the period $0 \le t \le T_{\rm EW}$. For convenience, we use a scaled time variable

$$\tilde{t} = \frac{t}{T_{\rm EW}} \tag{3.13}$$

In the present work, we assume that the function $f_V$ is given by the following function for the first period ($0 \le \tilde{t} < 1$)

$$f_V(\tilde{t}) = \begin{cases} \frac{\tilde{t}}{\tilde{T}_{\rm tran}}, & 0 \le \tilde{t} \le \tilde{T}_{\rm tran} \\ 1, & \tilde{T}_{\rm tran} \le \tilde{t} \le \tilde{T}_{\rm tran} + \tilde{T}_{\rm on} \\ 1 - \frac{\tilde{t} - (\tilde{T}_{\rm tran} + \tilde{T}_{\rm on})}{\tilde{T}_{\rm tran}}, & \tilde{T}_{\rm tran} + \tilde{T}_{\rm on} \le \tilde{t} \le 2\tilde{T}_{\rm tran} + \tilde{T}_{\rm on} \\ 0, & 2\tilde{T}_{\rm tran} + \tilde{T}_{\rm on} \le \tilde{t} < 1 \end{cases} \tag{3.14}$$

where $\tilde{T}_{\rm on}$ denotes the duration in which the voltage is maximum (scaled by $T_{\rm EW}$, called "fully-switched-on" time for convenience), $\tilde{T}_{\rm tran}$ denote the duration for transition (from no voltage to full voltage and vice versa, also scaled by $T_{\rm EW}$). Denoting the duration in which the voltage is zero as $\tilde{T}_{\rm off}$ (scaled by $T_{\rm EW}$), it is easy to find that $\tilde{T}_{\rm off} = 1 - \tilde{T}_{\rm on} - 2\tilde{T}_{\rm tran}$. Note that the unscaled durations are denoted as $T_{\rm on}$, $T_{\rm off}$, and $T_{\rm tran}$ (all measured in $T_c$), which can be obtained by multiplying the scaled ones with $T_{\rm EW}$.

For illustration, the instantaneous scaled voltage $f_V$ and contact angle $\theta(t)$ from Eq. (2.10) with the following parameters, $\theta(0) = 90°$, $\theta(V_M) = 135°$, $T_{\rm EW} = 100$, $\tilde{T}_{\rm tran} = 0.15(T_{\rm EW})$, and $\tilde{T}_{\rm on} = 0.5(T_{\rm EW})$ ($\tilde{T}_{\rm off} = 0.2(T_{\rm EW})$), are shown in Figure 3 for the first period. In subsequent periods, $f_V$ is easily specified from the periodic condition.

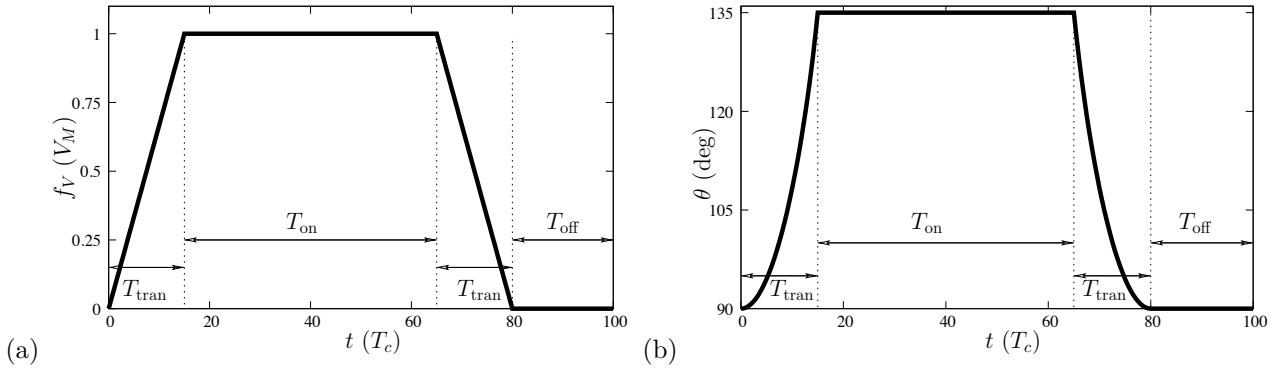


Figure 3: Evolutions of (a) the scaled voltage function $f_V$; (b) the dynamically imposed contact angle $\theta$. The parameters are $\theta(0) = 90°$, $\theta(V_M) = 135°$, $T_{\rm EW} = 100$, $\tilde{T}_{\rm tran} = 0.15(T_{\rm EW})$, and $\tilde{T}_{\rm on} = 0.5(T_{\rm EW})$ ($\tilde{T}_{\rm off} = 0.2(T_{\rm EW})$).

## 3.4 Validation

To validate the hybrid method and the code, a case of droplet dewetting (with much simpler EW control) has been simulated by the hybrid code (denoted as "Hybrid LBM-FVM") and another code that is based on the projection method (for the Navier-Stokes equations) (denoted as "NSCH PM"). In that code, a $2^{nd}$-order finite difference method was used for spatial discretization (of both the NSEs and CHE), $2^{nd}$-order semi-implicit Crank-Nicholson scheme and Adams-Bashforth scheme were used for the viscous term and the convection term in the momentum equation, respectively. In both methods, the $4^{th}$-order Runge-Kutta method was used for the time stepping of the CHE. For this validation case, the general parameters are $Re = 4000$, $Ca = 1$, $Cn = 0.15$, $Pe = 1.6 \times 10^4$, $S = 7.9 \times 10^{-3}$, $L_x \times L_y = 5 \times 2.5$, and the parameters for EW control are $\theta(0) = 90°$, $\theta(V_M) = 135°$, $T_{\rm tran} = 0$, and $T_{\rm on} \to \infty$ (which effectively correspond to a DC control). Note that initially (for

$t < 0$) the contact angle is 90° and the droplet is in static equilibrium with $R_x = R_{x,0}^{\text{stat}} = 1$. From $t = 0$, the imposed contact angle is suddenly changed to 135° and that causes the drop to retract.

Figure 4 compares the evolutions of $R_x$ for the period $0 \leq t \leq 1000$. It is seen that the evolutions of $R_x$ obtained by these two different numerical methods are close to each other. The droplet undergoes an initial oscillation with a rapidly decaying amplitude, and finally approaches an equilibrium state with $R_x \approx 0.545$. If the final contact angle is exactly 135°, the equilibrium value of $R(x)$ should be $R_{x,V_M}^{\text{stat}} = 0.524$, indicated by the horizontal dash-dot line in the plot. The small deviation from $R_{x,V_M}^{\text{stat}}$ can be attributed to numerical errors and the relatively large $Cn$ number.

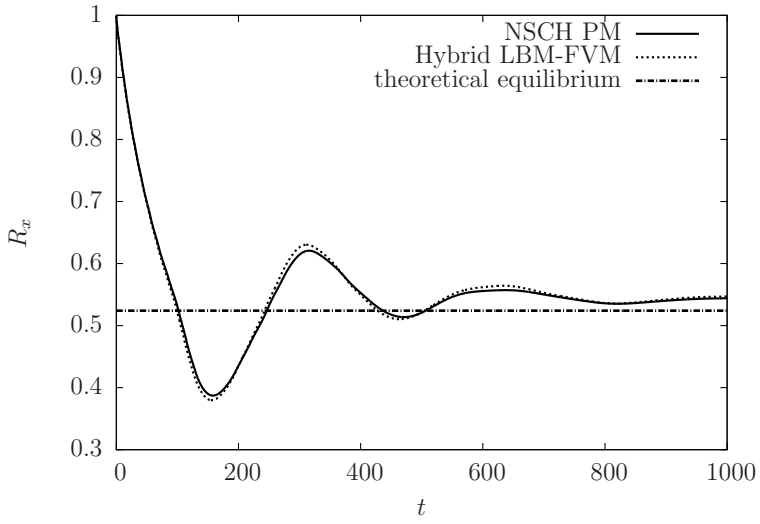


Figure 4: Comparison of $R_x$ evolutions by "NSCH PM" and "Hybrid LBM-FVM" with the same EW control. The horizontal line represents the final equilibrium value of $R_x$ based on theoretical estimate.

In Figure 5, we compare the velocity fields at t = 100 predicted by the two methods. Note that as implemented here, the two grids are offset by half a grid size. For example, in "NSCH PM" using finite difference, the wall overlaps with the boundary nodes, whereas in "Hybrid LBM-FVM" the wall is half-grid away from the outmost cell centers (note that it provides the integral along one side of these outmost cells in FVM). Therefore, the velocity vectors are plotted on staggered lattice points. But it is clear that the two velocity fields are in close agreement.

Finally, for this case (to finish $1000T_c$), the CPU times for "NSCH PM" and "Hybrid LBM-FVM" are 512 s and 303 s, respectively, on a PC with Intel Core Duo 1.83GHz CPU. This shows the advantage of the hybrid method. The relatively low speed of "NSCH PM" may be attributed to the cost of the solution of the Poisson equation for pressure and the semi-implicit time stepping.

### 3.5 Convergence toward Sharp-Interface Limit

A diffuse-interface computation should be done with a sufficiently thin interface such that the result does not depend on the interfacial thickness. Convergence to such a sharp-interface limit is typically established by numerical experiments with decreasing $W$ or $Cn$. For steady-state moving contact line problems, Yue et al. [18] showed that the sharp-interface limit is approached by decreasing the $Cn$ number while fixing other parameters. We follow a similar approach in our time-dependent problem. Specifically, we use $Pe = 4 \times 10^4$ and $S = 5 \times 10^{-3}$ in the convergence study. The $Cn$ number takes the following values 0.3, 0.15, 0.075 and 0.0375 in a series of simulations. Each simulation runs from 0 to 300. Other general parameters are $Re = 4000$, $Ca = 1$, $L_x \times L_y = 6 \times 3$. The EW control, as shown in Figure 3, is applied with the parameters listed again

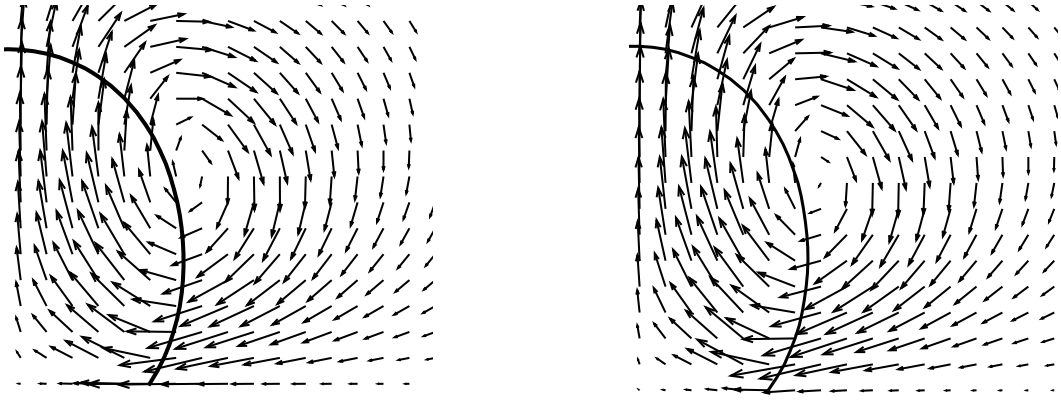

(a) (b)

Figure 5: Comparison of velocity fields (right half) around the interface at $t = 100$ by (a) "NSCH PM" and (b) "Hybrid LBM-FVM". For clarity, the velocity vectors are plotted every other grid point.

as follows, $\theta(0) = 90°$, $\theta(V_M) = 135°$, $T_{\rm EW} = 100$, $\tilde{T}_{\rm tran} = 0.15(T_{\rm EW})$, and $\tilde{T}_{\rm on} = 0.5(T_{\rm EW})$.

To examine the effects of varying $Cn$, we first investigate two quantities, the radius of the wetted area $R_x$ and the averaged vertical velocity of the drop $\bar{V}_d$. Figure 6 compares the evolutions of $R_x$ and $\bar{V}_d$ for different cases, and shows a clear trend of convergence as $Cn$ decreases. The difference in $R_x$ evolutions between $Cn = 0.075$ and $Cn = 0.0375$ is much smaller than that between $Cn = 0.15$ and $Cn = 0.075$. The same trend is seen for $\bar{V}_d$ as well. As noted before, the Reynolds number $Re$ given above ($Re = 4000$) does not actually reflect the physics of the problem; instead, it is defined based on a capillary velocity scale (Eq. 3.4). In actual simulations, as found in Figure 6, the maximum droplet velocity is about $2.5 \times 10^{-3}(U_c)$. Based on this value, one can estimate another set of dimensionless numbers as $Re_m \approx 10$ and $Ca_m \approx 2.5 \times 10^{-3}$, which more accurately reflect the flow magnitude of the problem. Unlike $Re$ and $Ca$, however, these depend on the EW control and cannot be determined a priori.

Besides the evolutions of $R_x$ and $\bar{V}_d$, interface positions at $t = 300$ are also compared. In Figure 7, the interface positions (defined as the contour lines with $\phi = 0$) are shown for different $Cn$ numbers. Note that because of the symmetry with respect to the center vertical line, only the right half is shown. Similar trend of convergence is also found from Figure 7 for decreasing $Cn$ number. Based on these results, we use $Cn = 0.075$ in the other results to be presented. This value provides a reasonably close approximation to the sharp-interface limit without incurring too much computational cost.

Though these figures are intended mostly for probing the sharp-interface limit, they also demonstrate some interesting physical behavior of the interface. Figure 6 shows that in the first three periods $R_x$ does not simply reflect the periodicity in the imposed contact angle (or the driving electrical field). Instead, between the first two periods, $R_x$ tends to decline, but climbs back up for the third period. After the first three periods, $R_x$ tends to become periodic. A prolonged run confirms that it eventually enters a periodic stage (as shown next). More analyses for longer runs will be provided later.

### 3.6 Droplet Motion under Electrowetting Control

Before proceeding to the detailed studies of EW controlled droplet, we list the common parameters for the simulations in Table 1. $N_{L,\rm dis}$ is the number of points to discretize the characteristic length $R$, $N_x \times N_y$ represent the discrete domain size, $N_{T,\rm dis}$ is the number of time steps to discretize the characteristic time $T_c$

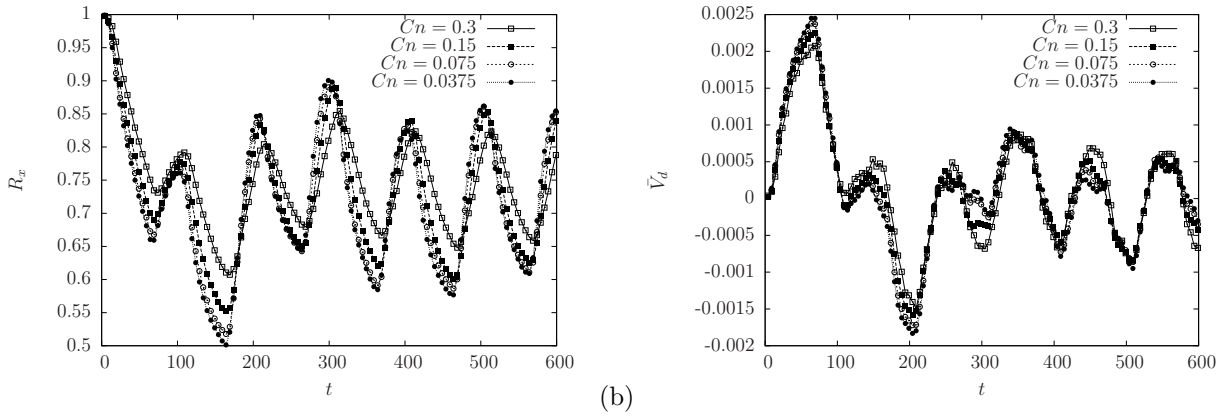


Figure 6: Convergence of the solution with decreasing $Cn$ manifested by (a) the evolution of $R_x$; and (b) the evolution of the average droplet velocity $\bar{V}_d$. The total time of 600 amounts to six periods of the electric voltage. Four $Cn$ numbers are tested: $Cn = 0.3$, 0.15, 0.075 and 0.0375, with $Pe = 4 \times 10^4$ and $S = 5 \times 10^{-3}$ fixed.

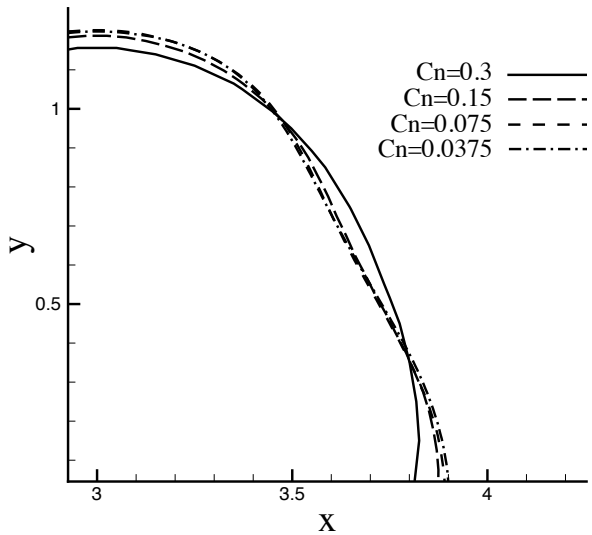


Figure 7: Comparison of interface positions at $t = 300$ with different $Cn$ numbers ($Cn = 0.3$, 0.15, 0.075 and 0.0375) at $Pe = 4 \times 10^4$ and $S = 5 \times 10^{-3}$.

(which means that the time step is $\frac{1}{N_{T,dis}}$ $(T_c)$). Let $T_t$ be the total simulation time (in $T_c$), then the total number of steps is $N_{T,\text{dis}} \times T_t$. $T_t$ may vary in different cases. We note that the $Pe$ number (or the $S$ number) is another independent parameter of the problem corresponding to the slip length in the sharp-interface model [18]. In this work, we do not intend to investigate its effects and focus on one specific $Pe$ (or $S$) only.

Table 1: Common parameters in simulations of EW controlled droplets

| Parameter | Value |
|---|---|
| $Re$ | 4000 |
| $Ca$ | 1 |
| $R$ | 1 |
| $L_x \times L_y$ | $6 \times 4$ |
| $Cn$ | 0.075 |
| $Pe$ | $4 \times 10^4$ |
| $S$ | $5 \times 10^{-3}$ |
| $N_{L,\text{dis}}$ | 40 |
| $N_x \times N_y$ | $240 \times 160$ |
| $N_{T,\text{dis}}$ | 160 |

In addition to those parameters given in Table 1, there are some others, including the set of parameters related to the EW control ($\theta(0)$, $\theta(V_M)$, $T_{\text{EW}}$, $\tilde{T}_{\text{tran}}$, and $\tilde{T}_{\text{on}}$). For simplicity, in this work $\theta(0)$ is fixed to be 90°, and we focus on the other parameters for the EW control.

#### 3.6.1 Analysis of typical droplet responses

Before varying the parameters, we examine the typical droplet responses to the applied electrical field. The case used in the convergence study is selected again for this purpose. The EW parameters are $\theta(0) = 90°$, $\theta(V_M) = 135°$, $T_{\text{EW}} = 100$, $\tilde{T}_{\text{tran}} = 0.15(T_{\text{EW}})$, $\tilde{T}_{\text{on}} = 0.5(T_{\text{EW}})$, and $\tilde{T}_{\text{off}} = 0.2(T_{\text{EW}})$. As briefly noted in Section 3.5, in the first few periods the droplet shows some irregular motions that do not match the imposed contact angle varying periodically. For a prolonged run with $0 \le t \le 1200$, which amounts to twelve periods of the voltage, the regular periodic motion is seen after about five periods, as reflected from the evolutions of $R_x$ and $\bar{V}_d$ shown in Figure 8. By comparing the *initial adjustment stage* (for this case approximately $0 \le t \le 500$) and the *periodic stage* (for this case $t > 500$), one may find the reason for the initial adjustment. In the *periodic stage*, $R_x$ varies regularly between maximum and minimum values, denoted as $R_{x,\max}$ and $R_{x,\min}$. It is seen that $R_{x,\min} > R^{\text{stat}}_{x,V_M}$ and $R_{x,\max} < R^{\text{stat}}_{x,0}$ where $R^{\text{stat}}_{x,0}$ and $R^{\text{stat}}_{x,V_M}$ are the static equilibrium values for DC control with no voltage and with full voltage applied, respectively (cf. Section 3.4). Thus, under periodic driving the drop never achieves the static conditions corresponding to zero and maximum voltages. This hints at an inertial effect at work.

Further understanding may be achieved by examining the detailed process in the two different stages. Figure 9 compares the interface evolutions during the $1^{st}$ and the $6^{th}$ periods at selected times. The local time $t'$ in Figure 9 is defined with respect to the start time of the $n^{th}$ period, i.e., $t' = t - (n-1)T_{\text{EW}}$. Although the local contact angle follows the same trend (cf. Figure 3b), the displacement of the contact line is different for the $1^{st}$ and $6^{th}$ periods, as is the overall interface shape. In the $6^{th}$ period, the interfaces at $t' = 0$ and $t' = 100$ almost overlap, as expected since the solution is in the *periodic stage*. At $t' = 0$ or 100, the drop assumes a non-circular shape and a negative velocity $\bar{V}_d$ (Figure 8b). By contrast, the initial shape in the $1^{st}$ period is circular and there is no flow at $t' = 0$. Therefore, although the external forcing on the contact line may be the same, the propagations of the capillary wave are different due to different initial configurations and flow fields. The initial adjustment hence represents the "correction", against inertia, of an initial condition that does not conform to the eventual periodic solution. We note that the division of droplet motion into two stages was also reported by Oh et al. [6]. In their numerical simulation of an oscillating droplet based on the domain perturbation method, an initial "stabilizing time", is required before harmonic drop deformation is established. Such observations

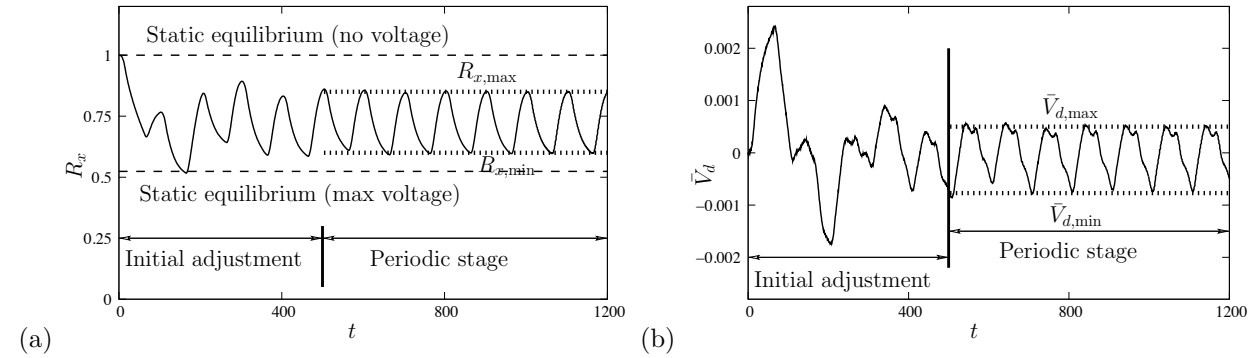


(a) (b)

Figure 8: Evolution of (a) the radius $R_x$ of the contact line and (b) the drop velocity $\bar{V}_d$ in $0 \leq t \leq 1200$ for the case with $\theta(0) = 90°$, $\theta(V_M) = 135°$, $T_{\rm EW} = 100$, $\tilde{T}_{\rm tran} = 0.15(T_{\rm EW})$, $\tilde{T}_{\rm on} = 0.5(T_{\rm EW})$, and $\tilde{T}_{\rm off} = 0.2(T_{\rm EW})$

agree with the present numerical results qualitatively even though the specific setup, the models and methods are different.

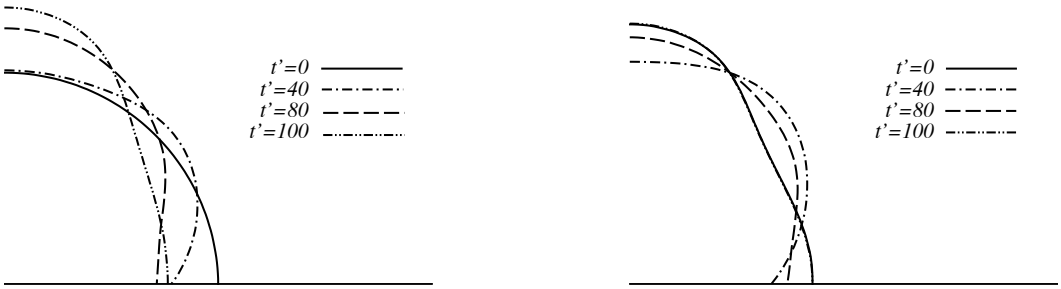


(a) (b)

Figure 9: Snapshots of interface positions at selected times ($t' = 0,\ 40,\ 80,\ 100$) during (a) the $1^{st}$ period (*initial adjustment stage*) and (b) the $6^{th}$ period (*periodic stage*) for the case with $\theta(0) = 90°$, $\theta(V_M) = 135°$, $T_{\rm EW} = 100$, $\tilde{T}_{\rm tran} = 0.15(T_{\rm EW})$, $\tilde{T}_{\rm on} = 0.5(T_{\rm EW})$, and $\tilde{T}_{\rm off} = 0.2(T_{\rm EW})$. Note that in (b) the interfaces at $t' = 0$ and $t' = 100$ almost overlap (as required by the periodicity).

### 3.6.2 Effects of control period $T_{\rm EW}$ and "fully-switched-on" time $\tilde{T}_{\rm on}$

First, $T_{\rm EW}$ and $\tilde{T}_{\rm on}$ are investigated with $\theta(V_M)$ fixed at 135°. Five values for $T_{\rm EW}$ were tested: $T_{\rm EW} = 100$, 200, 300, 400, and 600. In these cases, we keep $T_{\rm tran} = 15$ fixed, such that its fraction of $T_{\rm EW}$ varies. For each $T_{\rm EW}$, different values of $\tilde{T}_{\rm on}$ were investigated. Note that $\tilde{T}_{\rm off} = 1 - \tilde{T}_{\rm on} - 2\tilde{T}_{\rm tran}$, thus the ratio $\frac{\tilde{T}_{\rm on}}{\tilde{T}_{\rm off}}$ (equal to $\frac{T_{\rm on}}{T_{\rm off}}$) varies with $\tilde{T}_{\rm on}$ for given $T_{\rm EW}$ and $T_{\rm tran}$. The specific cases tested for each $T_{\rm EW}$ are summarized in Table 2.

First, we fixed $\frac{T_{\rm on}}{T_{\rm off}} = 1$ and varied the length of $T_{\rm EW}$. The initial adjustment stage, measured in $T_{\rm EW}$, shortens as the period $T_{\rm EW}$ increases. In the following, we focus on the periodic stage. Figure 10 compares the $R_x$ evolutions during $400 \leq t \leq 1600$ for the five $T_{\rm EW}$ values. In all cases, $R_x$ displays a periodic variation with the period matching that of the applied voltage. The most prominent feature of Figure 10 is resonance at $T_{\rm EW} = 300$. The amplitude of $R_x$ oscillation at this period is larger than those for shorter and longer periods. This is more clearly demonstrated in Figure 11 that plots $(R_{x,\max} - R_{x,\min})$ as a function of $T_{\rm EW}$. The existence

Table 2: Temporal control parameters for different cases. The first three columns are given in $T_c$.

| $T_{\rm EW}$ | $T_{\rm on}$ | $T_{\rm off}$ | $\frac{T_{\rm on}}{T_{\rm off}}$ |
|---|---|---|---|
| 100 | 5 | 65 | 0.08 |
| | 10 | 60 | 0.17 |
| | 35 | 35 | 1.0 |
| | 50 | 20 | 2.5 |
| | 60 | 10 | 6.0 |
| | 65 | 5 | 13.0 |
| 200 | 20 | 150 | 0.13 |
| | 85 | 85 | 1.0 |
| | 150 | 20 | 7.5 |
| 300 | 90 | 180 | 0.5 |
| | 135 | 135 | 1.0 |
| | 180 | 90 | 2.0 |
| | 240 | 30 | 8.0 |
| 400 | 40 | 330 | 0.12 |
| | 185 | 185 | 1.0 |
| | 330 | 40 | 8.25 |
| 600 | 60 | 510 | 0.12 |
| | 285 | 285 | 1.0 |
| | 510 | 60 | 8.5 |

of resonance frequency for AC-controlled droplets has been reported previously by Oh et al. [6] for a sinusoidal voltage and by Lai et al. [12] for square waves. Our results show resonance for a trapezoid waveform, the limit of which, when $T_{\rm tran} \to 0$, corresponds to the periodic square wave.

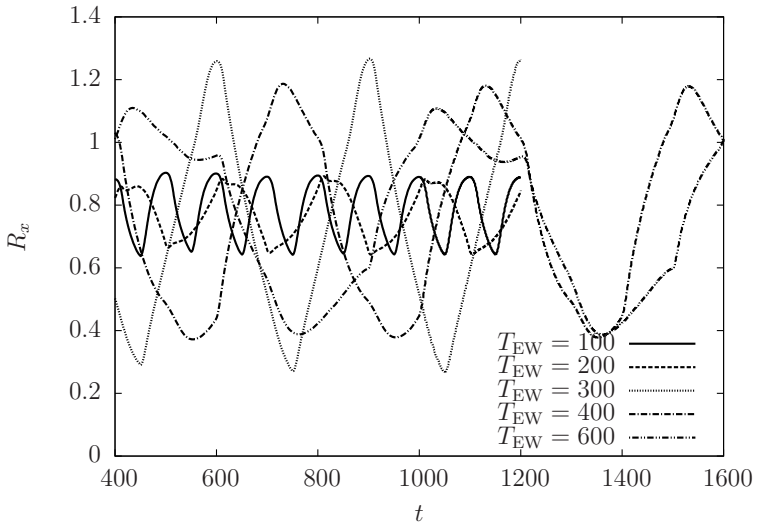


Figure 10: Evolutions of $R_x$ for $\tilde{T}_{\rm on} = \tilde{T}_{\rm off}$ with $T_{\rm EW} = 100,\ 200,\ 300,\ 400$, and 600.

The resonance can be understood from the "reaction time" of the sessile drop to external forcing. Note that the problem involves three time scales: the droplet's intrinsic relaxation time (sometimes called the "emulsion time"), the reaction time of the sessile drop, and the driving period. The emulsion time $T_c$ (see Eq. (3.5)), which reflects how fast the droplet shape reacts to disturbance, is small and should be irrelevant here. The reaction time of the sessile droplet reflects how fast the drop contracts or spreads on the substrate when the contact angle is changed. Dominated by the viscous friction at the contact line, it should be much larger than $T_c$ but is

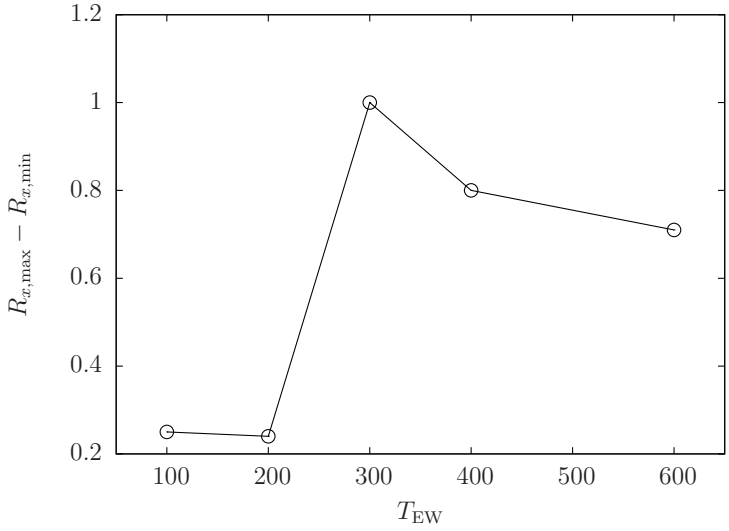


Figure 11: Variations of $R_{x,\max} - R_{x,\min}$ with $T_{\rm EW}$ at $\tilde{T}_{\rm on} = \tilde{T}_{\rm off}$.

difficult to estimate more quantitatively. In experiments, contact angle hysteresis will also affect this reaction time. In any event, resonance is expected when the driving period of the voltage approaches the reaction time of the sessile drop. Interestingly, Oh et al. [6] and Lai et al. [12] both reported resonance at multiple driving frequencies, indicating that different modes of shape oscillation have different resonance frequencies. Figure 11 shows a single resonance period, probably owing to the narrow range explored in our simulations.

Next, we investigate the effects of varying the fractions of $\tilde{T}_{\rm on}$ and $\tilde{T}_{\rm off}$ within a fixed $T_{\rm EW}$. For $T_{\rm EW} = 100$, Figure 12 compares the evolutions of $R_x$ for $\tilde{T}_{\rm on} = 0.05,\ 0.1,\ 0.35,\ 0.5,\ 0.6,\ 0.65$ for the interval $0 \le t \le 600$. In all cases, the droplet enters the periodic stage after an initial adjustment of three to five $T_{\rm EW}$. With increasing $\tilde{T}_{\rm on}$, the droplet dewets more (corresponding to smaller $R_{x,\min}$) as one might expect.

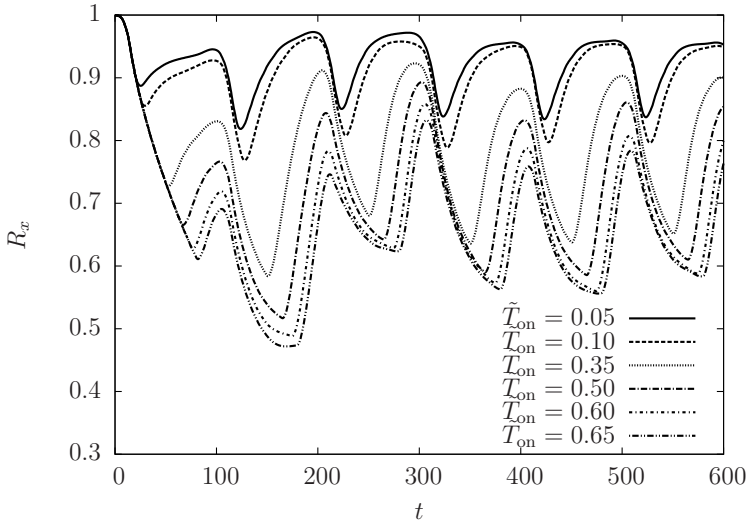


Figure 12: Evolutions of $R_x$ with $T_{\rm EW} = 100$, and $\tilde{T}_{\rm on} = 0.05$, 0.1, 0.35, 0.5, 0.6, and $0.65(T_{\rm EW})$

Figure 13 plots the amplitude ($R_{x,\max} - R_{x,\min}$) against the ratio $\frac{T_{\rm on}}{T_{\rm off}}$ for different values of $T_{\rm EW}$. In all cases, the amplitude of droplet oscillation peaks at $\frac{T_{\rm on}}{T_{\rm off}} = 1.0$, the effect being most prominent at the resonance period ($T_{\rm EW} = 300$). Equal duration of the spreading and dewetting stages is conducive to larger amplitude

of oscillation. When the two durations are made unequal, for instance by increasing $\tilde{T}_{\text{on}}$, the droplet dewets more during the "on" stage but the extra displacement cannot be fully recovered during the "off" stage, thereby limiting the amplitude. This finding may be important to the control of droplets using EW to achieve more energetic oscillation and hence more efficient mixing inside.

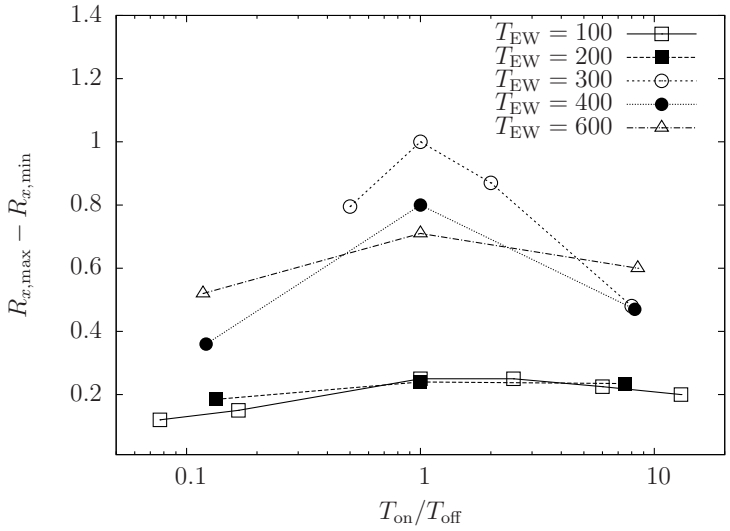


Figure 13: Variations of $R_{x,\max} - R_{x,\min}$ with $\frac{T_{\text{on}}}{T_{\text{off}}}$ at $T_{\text{EW}} = 100$, 200, 300, 400, and 600.

### 3.6.3 Effects of control force $\theta(V_M)$

Besides the temporal control parameters discussed above ($T_{\text{EW}}$ and $\tilde{T}_{\text{on}}$), we have also investigated $\theta(V_M)$ as an indication of the *magnitude* of the EW forcing. For this study, the following temporal parameters were used: $T_{\text{EW}} = 300$ and $\tilde{T}_{\text{on}} = \tilde{T}_{\text{off}} = 0.45(T_{\text{EW}})$. Figure 14 shows the temporal evolutions of $R_x$ for $\theta(V_M)$ ranging from 120° to 140°. With increasing $\theta(V_M)$, the amplitude of oscillation increases, as expected. $R_x$ retains the same regular zigzag pattern in time. We did not investigate if the resonance period varied with $\theta(V_M)$. The experimental study of Oh et al. [6] reported that the resonance frequency decreases slightly with increasing maximum voltage. Figure 15 plots the amplitude of oscillation $R_{x,\max} - R_{x,\min}$ as a function of the contact angle difference $\theta(V_M) - \theta(0)$ at zero and maximum voltages. Increasing the magnitude of the driving force causes an increase in the amplitude of drop oscillation. Within the range tested, this relationship is approximately linear.

# 4 Concluding Remarks

To summarize, a hybrid LBM-FVM numerical model based on phase-field theory has been developed for electrowetting problems, and validated through comparisons with other methods. Application of this new method to electrowetting of droplets controlled by AC voltage has identified two stages of droplet deformation: an initial adjustment stage and a periodic stage. This study has also revealed the effects of the control parameters. In particular, to achieve the most energetic droplet oscillation, a resonance period has been found for the driving voltage, together with an optimal on-off time ratio within the period. Besides, the effects of the magnitude of the control force have also been examined. The droplet oscillation amplitude varies roughly linearly with the change in contact angle due to the maximum voltage. These results suggest a strategy to control the parameters of the problem to achieve highly efficient mixing within the droplet.

It should be noted that the present work has several limitations. First, the problem considered is two-dimensional and the droplet actually corresponds to an infinitely long ridge. To match with real experiments, axisymmetric

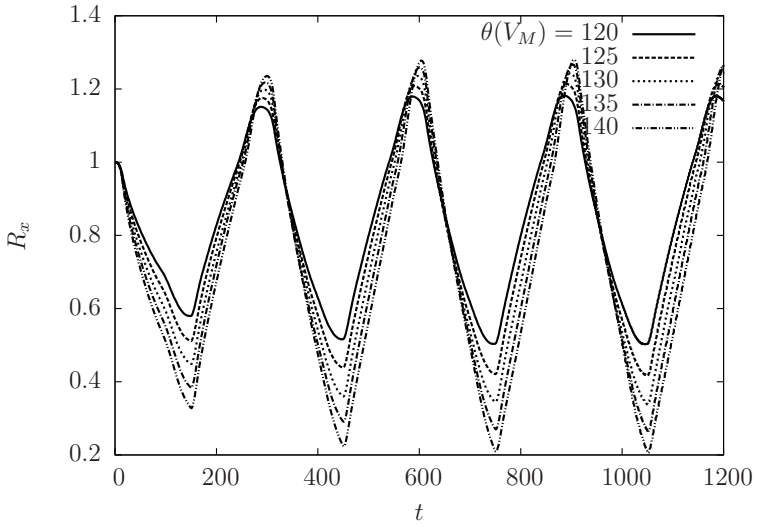


Figure 14: Evolutions of $R_x$ for $T_{\rm EW} = 300$, $\tilde{T}_{\rm on} = \tilde{T}_{\rm off} = 0.45(T_{\rm EW})$ with $\theta(V_M) = 120^\circ,\ 125^\circ,\ 130^\circ,\ 135^\circ$, and $140^\circ$.

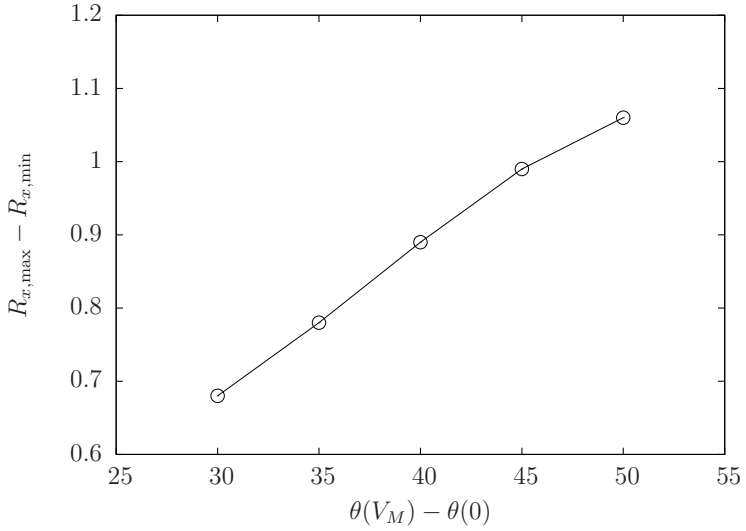


Figure 15: Variation of $R_{x,\max} - R_{x,\min}$ with $\theta(V_M) - \theta(0)$ for $T_{\rm EW} = 300$, $\tilde{T}_{\rm on} = \tilde{T}_{\rm off} = 0.45(T_{\rm EW})$.

or, more generally, three-dimensional simulations are required. Second, we have used a simple model for electrowetting (EW), which mimics EW by varying the imposed static contact angle. As noted before, this neglects changes of material properties after the voltage is applied, and assumes that the action of voltage is instant and the system can achieve local equilibrium also instantly. Such assumptions may be well justified for DC-controlled EW systems. For AC-controlled EW they are less so. For example, a recent experimental study [12] found that the phase difference between the droplet motion and the applied voltage varies (from $-180°$ to $180°$) with the frequency of the voltage. A better model should take into account such factors. Third, the two fluids were assumed to have the same density and viscosity. Although this is close to some experiments using liquid-liquid systems (e.g., see [10]), it differs much from the common situation of water droplets in air. The roles of the density and viscosity ratios in the EW systems need to be studied further. Finally, the contact angle hysteresis (CAH) is not yet considered in the modeling. Thus, this study corresponds to *perfectly smooth* surfaces without CAH. The inclusion of CAH might improve the prediction of EW by introducing phase difference between the droplet response and the applied voltage. However, currently it is an unresolved issue in contact line models.

# References


[1] T. M. Squires and S. R. Quake, *Rev. Mod. Phys.* **77**, 977 (2005).

[2] M. G. Pollack, R. B. Fair and A. D. Shenderov, *Appl. Phys. Lett.* **77**, 1725 (2000).

[3] M. G. Pollack, A. D. Shenderov and R. B. Fair, *Lab Chip* **2**, 96 (2002).

[4] J. Lienemann, A. Greiner and J. G. Korvink, *IEEE Trans. Comput.-Aided Design Integr. Circuits Syst.* **25**, 234 (2006).

[5] S. W. Walker, B. Shapiro and R. H. Nochetto, *Phys. Fluids* **21**, 102103 (2009).

[6] J. M. Oh, S. H. Ko and K. H. Kang, *Langmuir* **24**, 8379 (2008).

[7] J. M. Oh, S. H. Ko and K. H. Kang, *Phys. Fluids* **22**, 032002 (2010).

[8] H.-W. Lu, K. Glasner, A. L. Bertozzi and C.-J. Kim, *J. Fluid Mech.* **590**, 411 (2007).

[9] H. Aminfar and M. Mohammadpourfard, *Comput. Methods Appl. Mech. Engrg.* **198**, 3852 (2009).

[10] F. Mugele, J.-C. Baret and D. Steinhauser, *Appl. Phys. Lett.* **88**, 204106 (2006).

[11] S. H. Ko, H. Lee and K. H. Kang, *Langmuir* **24**, 1094 (2008).

[12] M.-F. Lai, C.-P. Lee, C.-N. Liao and Z.-H. Wei, *Appl. Phys. Lett.* **94**, 154102 (2009).

[13] S. H. Ko, S. J. Lee and K. H. Kang, *Appl. Phys. Lett.* **94**, 194102 (2009).

[14] P. Paik, V. K. Pamula, M. G. Pollack and R. B. Fair, *Lab Chip* **3**, 28 (2003).

[15] P. Paik, V. K. Pamula and R. B. Fair, *Lab Chip* **3**, 253 (2003).

[16] H. W. Zheng, C. Shu and Y. T. Chew, *J. Comput. Phys.* **218**, 353 (2006).

[17] A. Tiribocchi, N. Stella, G. Gonnella and A. Lamura, *Phys. Rev. E* **80**, 026701 (2009).

[18] P. Yue, C. Zhou and J. J. Feng, *J. Fluid Mech.* **645**, 279 (2010).

[19] J. J. Huang, C. Shu and Y. T. Chew, *Int. J. Numer. Meth. Fluids* **60**, 203 (2009).

[20] D. Jacqmin, *J. Comput. Phys.* **155**, 96 (1999).

[21] V. V. Khatavkar, P. D. Anderson and H. E. H. Meijer, *J. Fluid Mech.* **572**, 367 (2007).